Finite Difference Time Domain Calculation on Layer-by-Layer Assemblies of Close-Packed Gold Nanoparticles

Min Kyung Oh[1], Sungho Park[1,2], Seong Kyu Kim[1,*], and Sang-Hyun Lim[3]

[1] *Department of Chemistry,* [2] *Department of Energy Science, and SKKU Advanced Institute of Nanotechnology, Sungkyunkwan University, Suwon, 440-746, Republic of Korea*
[3] *Department of Chemistry and Biochemistry, The University of Texas at Austin, Austin, TX 78712-0165, USA*

The finite difference time domain (FDTD) method was applied to obtain transmission spectra and local electric field distributions for layer-by-layer assemblies of close-packed gold nanospheres (NSs) and gold nanorods (NRs). The computational results were used to understand variations in the extinction spectra and in the surface enhanced Raman scattering (SERS) for the corresponding experimental samples. High local electric fields were found at small interstices among neighboring nanoparticles. In general, the sum of the local field intensities of the so-called 'hot spots' in a layer was greater in the NR assemblies than in the NS assemblies. Furthermore, high local electric fields, polarized along the light propagation direction, were found at the interlayers of the NR assemblies, while they were small in the NS assemblies. These results are in accord with the SERS results and can be explained in large part by the greater contact area in the NR assemblies than in the NS assemblies. However, the calculated local fields for the multilayer assemblies were limited to the top few layers while the interlayer couplings were significantly reduced at the lower layers, as the incident light was extinguished mostly at the top few layers. Such a layer-by-layer local field distribution was insufficient to explain the SERS intensity variation with the number of layers. Implications of the mismatch and possible limitations of the computations will be discussed.

Keywords: Finite Difference Time Domain, FDTD, Local Field, Gold, Nanoparticle, Plasmon, Surface Enhanced Raman Scattering, SERS, Interlayer Coupling.

**RESEARCH ARTICLE**

1. INTRODUCTION

Noble metals in nanometer domains exhibit colors due to localized surface Plasmon resonance (LSPR) in the visible region. LSPR also induces extremely high local electric fields in certain noble metal nanostructures, such as sharp features or interparticle gaps.[1–5] This phenomenon is considered a primary process for surface enhanced Raman scattering (SERS).

Numerous nanostructures, mostly of gold or silver, have been studied to elucidate the behavior of LSPR and its relation with SERS. Among them are the unique close-packed gold nanoparticle films that this lab has recently developed.[6–11] The film was produced by collecting gold nanoparticles at a water–nonpolar liquid interface, followed by transferring the film onto a solid substrate. This film has shown several characteristics suitable for an excellent

SERS substrate. First, by repeating the transfer process, a layer-by-layer assembly was possible. Accordingly, nanoparticles of numerous shapes have been assembled into multilayers; multilayer films with gold nanospheres (NSs) in the diameter range of 5∼30 nm and gold nanorods (NRs) of similar diameters with various aspect ratios have been demonstrated. Second, as nanoparticles in each layer were packed with a density close to a theoretical maximum, an extremely high density of interparticle gaps or purported 'hot-spots' was generated. Third, surfactant molecules used to stabilize the nanoparticles in solution were largely uncapped during the film formation process, so that the SERS spectra were free of peaks from such impurities.[6,7]

General features of the closed-packed gold nanoparticle films produced in this lab[6–11] are illustrated in Figure 1. Figure 1(a) is the scanning electron microscope (SEM) image of one monolayer (ML) film of the close-packed gold NSs with a diameter of 21.5 (±2.3) nm, while

*Author to whom correspondence should be addressed.
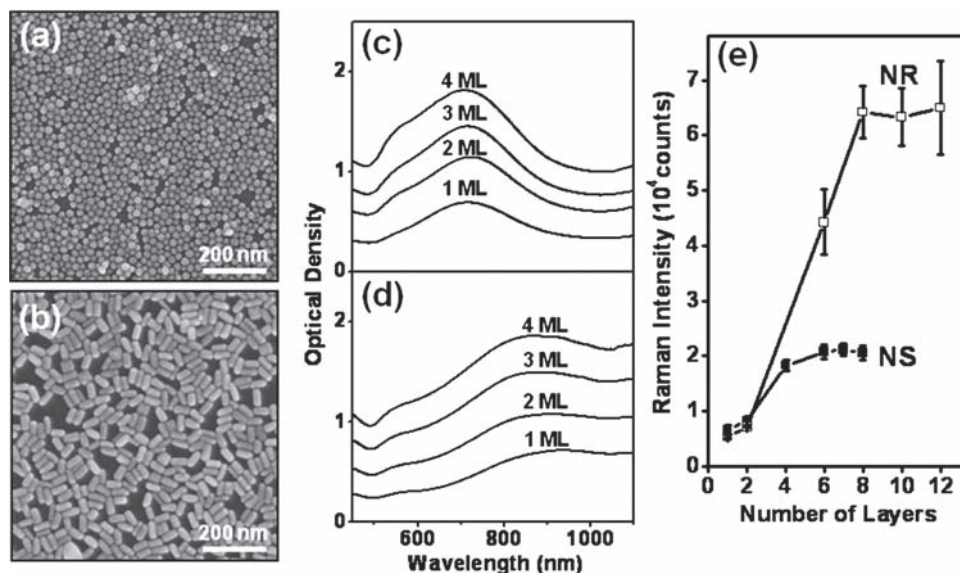
Fig. 1. Examples of the SEM images (a and b), the excitation spectra (c and d), and the variation in SERS intensity with the number of layers (e). (a) and (c) are for films assembled with NSs with a diameter of 21.5 (±2.3) nm. (b) and (d) are for films assembled with NRs with a diameter of 24.0 (±1.6) nm and a length of 53.5 (±3.3) nm. In (e), □ is for the NR film series and ■ for the NS film series.

Figure 1(b) is the SEM image of the 1 ML film of gold NRs with a diameter of 24.0 (±1.6) nm and a length of 53.5 (±3.3) nm. In the NS film, the NSs were well packed within most of the area, giving a typical surface packing efficiency of about 80%, smaller than but close to that of two-dimensional hexagonal closest packing (90.7%). In the NR film, most of the NRs were lying flat on the film plane and packed with almost the same surface packing efficiency as the NS film. Figures 1(c and d) are the extinction spectra of the NS and NR films as the number of layers were varied. A broad LSPR band appeared around 600~800 nm for the NS films and 700~1000 nm for the NR films.

Variations in the SERS intensities with the number of layers are shown in Figure 1(e). Here, the plotted SERS intensities correspond to a C–C stretching vibration peak at 1572 cm^{-1} for the benzenethiol analyte. The excitation wavelength for the SERS experiments was 632.8 nm. The trend shown Figure 1(e) is typical of the film series produced employing the method developed and presented herein:

(1) the film packed with NRs generated higher SERS signal than that with NSs of the same diameter;[7, 10]

(2) in a given series, the SERS signal increased almost linearly with the number of layers until a saturation layer (approximately 5 ML for the NS films and 7 ML for the NR films) was reached,[6, 7, 10, 11] implying that every single layer in the multilayer film contributed almost equally to the SERS signal;

(3) from this lab's recent investigation,[10] the structure of the top layer was critical while that of lower layers was much less important in determining SERS intensity.

These observations suggest that a three-dimensional nanoscale architecture can be a more efficient SERS substrate and should be studied systematically, while most SERS studies thus far have focused on two-dimensional systems.

To understand the details of light-matter interactions in the three-dimensional nanostructures, we employed a computational method called the finite difference time domain (FDTD) calculation.[12, 13] The FDTD method is designed to determine the time-domain solutions of Maxwell's curl equations for a given spatial distribution of optical constants of a test system whose space is finely divided by Cartesian grid cells. Provided with a source of an electromagnetic field at a designated space, the FDTD algorithm implements a stepwise time-evolution of changes in an electric (or magnetic) field at each grid cell to variations in a magnetic (or electric) field at its neighboring cells.[10]

As the FDTD method is fully explicit unlike other methods that use linear algebra, application of this method is virtually unlimited to the size of the test system, as long as the step resolution can compromise the memory capabilities of a computer. In this respect, FDTD is the suitable method to computationally reproduce the optical properties of the nanostructures presented herein, where a large size target (due to lateral dimensions of the film) should be calculated with an ultrafine spatial resolution (to reflect the small interparticle gaps). Simulating the experimental system currently employed requires that an incident light is generated externally and propagated through a target space; the FDTD method works in this way. A resulting spectrum of the light-matter interactions can be obtained in a single run where a broadband pulsed light is propagated and its flux detected at a designated area is Fourier-transformed.

The local field at each grid cell can be obtained by time-averaging the electric field intensities for a fixed frequency of incident light.

The LSPR phenomena can be studied by the FDTD method if the optical dispersion of the test material is known. For example, the optical properties of numerous gold or silver nanostructures, such as single, dimeric, or trimeric nanoparticles,[15–19] one-dimensional nanoparticle chains,[20, 21] two-dimensional nanoparticle arrays,[22] or core–shell structures,[23, 24] have been successfully studied using the FDTD method with bulk dispersion relations of the target material. The target structure presented herein is three-dimensional and much larger than the above examples. Monitoring in an ultrafine resolution is thus required; the FDTD method meets this challenge for its effectiveness.

2. COMPUTATIONAL METHODS

2.1. Lattice Space and Target

For the FDTD calculations, a MEEP program (version 0.20.3), developed by Johnson,[25] was used. The lattice space of the calculation is summarized in Figure 2. Along the light propagating *z*-axis, 300 nm thick perfect matching layers (PML)[25] were placed at both ends. Free spaces (1.0 μm thick) were placed below the top PML and above the bottom PML. In between these two free spaces, the target space was placed. An electromagnetic light source was set 30 nm below the top PML, which was propagated as a plane-wave along the *z*-axis. A periodic boundary condition was applied to all *x*-, *y*-, and *z*-axes, so that the target structure was a repeating unit of an infinitely large two-dimensional film.

The *xy* size of the lattice space was varied with the target structure. Here, three different target structures were calculated for: (1) hexagonal closest packing of spheres (HS); (2) random loose packing of spheres (LS); (3) random loose packing of rods (LR). For the HS assemblies, twelve gold spheres of 20 nm diameter were packed with a contact spacing of 1 nm. Contact spacing is the minimum distance between any two neighboring nanoparticles. This afforded a *xy* lattice dimension of 63×73 nm^2. For a multilayer HS assembly, spheres of an upper layer were arranged to sit at the three-fold interstitial sites of the lower layer spheres, shifted up by $(\sqrt{3}/2) \times 21$ nm, so that an ABC type hexagonal closest packing was achieved. For the LS assemblies, fifty-one or fifty-two 20 nm diameter spheres were packed randomly within 150×150 nm^2. A contact spacing of 1 nm was also placed between any neighboring spheres. Here, spheres at the *x* or *y* boundaries were arranged to satisfy the periodic boundary conditions. In the LS assemblies, the surface packing efficiency was 71.2 or 72.6%, somewhat smaller than that of the experimental films. For a multilayer LS assembly, spheres in each layer were arranged independently and placed up
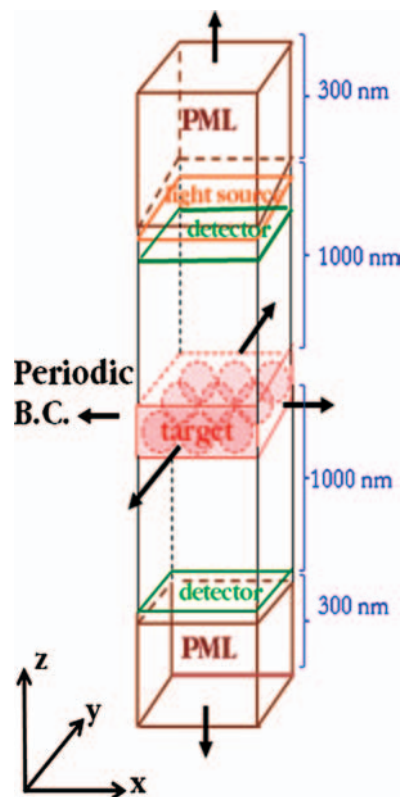

Fig. 2. Structure of the space used for MEEP calculation.

or down, 21 nm from the lower or upper layer. For the LR assemblies, forty or forty-one rods of 20 nm diameter and 41 nm length (counting semispherical caps) were packed randomly within 200×200 nm^2. A contact spacing of 1 nm was also set. Here, the rods at the *x* or *y* boundaries were arranged to satisfy the periodic boundary conditions. In the LR assemblies, the surface packing efficiency was 73.4 or 75.3%, somewhat smaller than that of the experimental films. For a multilayer LR, rods in each layer were arranged independently and placed up or down, 21 nm from the lower or upper layer.

For the dispersion equation of optical constants of gold, the complex dielectric constant data of Johnson and Christy[27] were used to fit Eq. (1), based on an extended Drude model:[28]

$$\epsilon(\omega) = \epsilon_\infty - \frac{A}{\omega^2 + i\gamma_D\omega} - \frac{B\gamma_L^2}{\omega^2 - \omega_L^2 + i\gamma_L\omega} \qquad (1)$$

With fitting parameters similar to those in Ref. [28], an excellent fit of $\epsilon(\omega)$ to Johnson and Christy's data was made in the wavelength range between 500 and 2000 nm. For the dielectric constants of the interface cells between the gold and free cells, a subpixel smoothing[29] was used.

For all the target structures, up to four monolayers were calculated with a grid cell dimension of $1 \times 1 \times 1$ nm^3. For the largest target structure, a 4 ML of the LR, the number of grid cells was 107,360,000 ($= 200 \times 200 \times (2600 + 4 \times 21)$). As the calculation for this many grid cells

required a computational memory over 45 GB, a parallel computer system (32 nodes, 2 CPU and 2 GB in each node) was employed.

2.2. Spectra

In order to obtain the spectrum of a target, a detector was placed 50 nm above the bottom PML to monitor the transmission flux. Marching of an electromagnetic wavepacket was initiated with a pulsed light source with a Gaussian band (FWHM = 2.1 μm^{-1} centered at 1.4 μm^{-1}). The time-varying flux was recorded until the electric field at the detector decayed to 0.2% of its maximum. This process required approximately 5 to 10 time units (TU, 1 TU = 3.333 fs), depending on the target structure. The time profile of the detected flux was then Fourier-transformed to give the transmission spectrum. The spectrum in the absence of a target was used for its normalization. The spectra for x-polarized light and y-polarized light were obtained separately and averaged to give a spectrum for unpolarized light.

## 2.3. $\langle \mathbf{E}^2 \rangle$ Distribution

In order to obtain $\langle \mathbf{E}^2 \rangle$ distribution around a target, the wave propagation was initiated with a continuous wave light source at a fixed wavelength (632.8 nm), polarized along the x or y direction. After 6 TU (=20 fs), each x, y, z component of the electric field at the grid cells of the target space were recorded at 0.2 TU intervals. The recording continued until 12 TU (=40 fs) were reached. At this end, $\langle \mathbf{E}^2 \rangle$ at each grid cell was calculated as the time average of $\mathbf{E}_x^2 + \mathbf{E}_y^2 + \mathbf{E}_z^2$. In the absence of a target, the average was 0.125, which was used to normalize $\langle \mathbf{E}^2 \rangle$.

3. RESULTS AND DISCUSSION

3.1. Spectra

Figure 3 is the optical density spectra of the three target structures, obtained at the transmission detector. The ordinate is $-\log(I(C))/I_0(C)$, where $I(C)$ and $I_0(C)$ are the intensities of the Fourier-transformed spectra in the presence and absence of a target, respectively. Therefore, the spectra of Figure 3 may be compared to the extinction spectra in Figures 1(c and d).

In the simulated spectra for the HS and the LS assemblies, the LSPR band appeared at wavelengths around 600 nm. The LSPR band of the HS assemblies is red-shifted from that of the LS assemblies, in accordance with our experimental observation that a higher degree of the packing shifts the resonance wavelength to the red. The LSPR band in the experimental spectra (Fig. 1(c)) is red-shifted and much broader, compared to that in the corresponding simulated spectra. Part of this discrepancy may
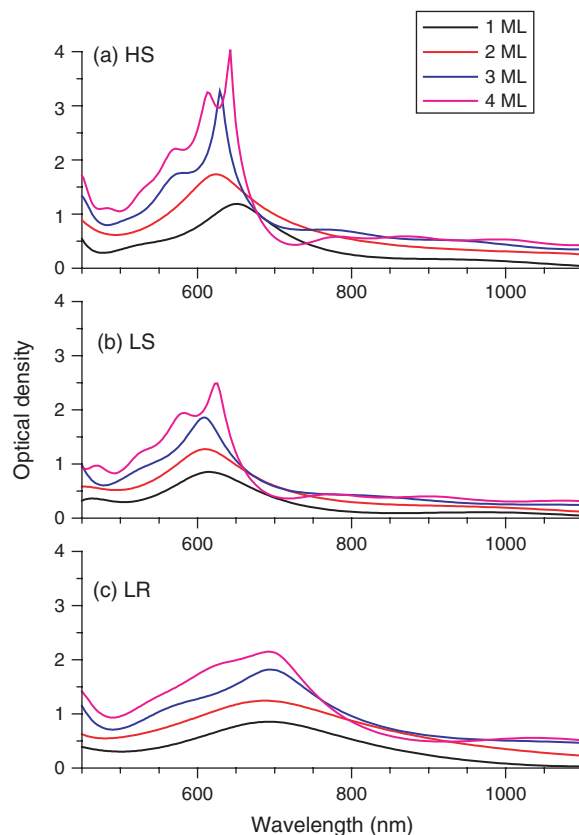
Fig. 3. Transmission spectra from the FDTD calculation: (a) hexagonal closest packing of spheres of 20 nm diameter; (b) random loose packing of spheres of 20 nm diameter; (c) random loose packing of rods of 20 nm diameter and 41 nm length. For each target structure, spectra of up to 4 ML were calculated.

be due to dispersion in the particle sizes in the experimental films. In addition, the target structures in the calculation had a two-dimensional repeating unit due to the periodic boundary conditions, which may have developed sharp features as a computational artifact.

The LSPR band in the simulated spectra for the LR assemblies appeared at wavelengths longer than those for the HS or the LS assemblies; this is in agreement with the trend in the experimental spectra. However, the wavelengths were shorter by 100∼200 nm than those in the experimental spectra. Part of this discrepancy can be explained by the fact that the NRs in Figure 1 were longer than the NRs in the simulation and that the NRs in the experiments were arranged side-by-side more than in the simulation.

In the simulated spectra for both the NS and NR assemblies, the background plateau in the experimental spectra was not apparent. The background plateau increased sharply in the experimental spectra as the wavelength dropped below 450 nm. This behavior is assignable to an interband transition of gold. According to an analysis of Hao and Norlander,[24] the dielectric constant of Eq. (1), or the extended Drude model, does not reproduce features

of the interband transition, while the model is still good to predict the LSPR bands at wavelengths longer than 500 nm.
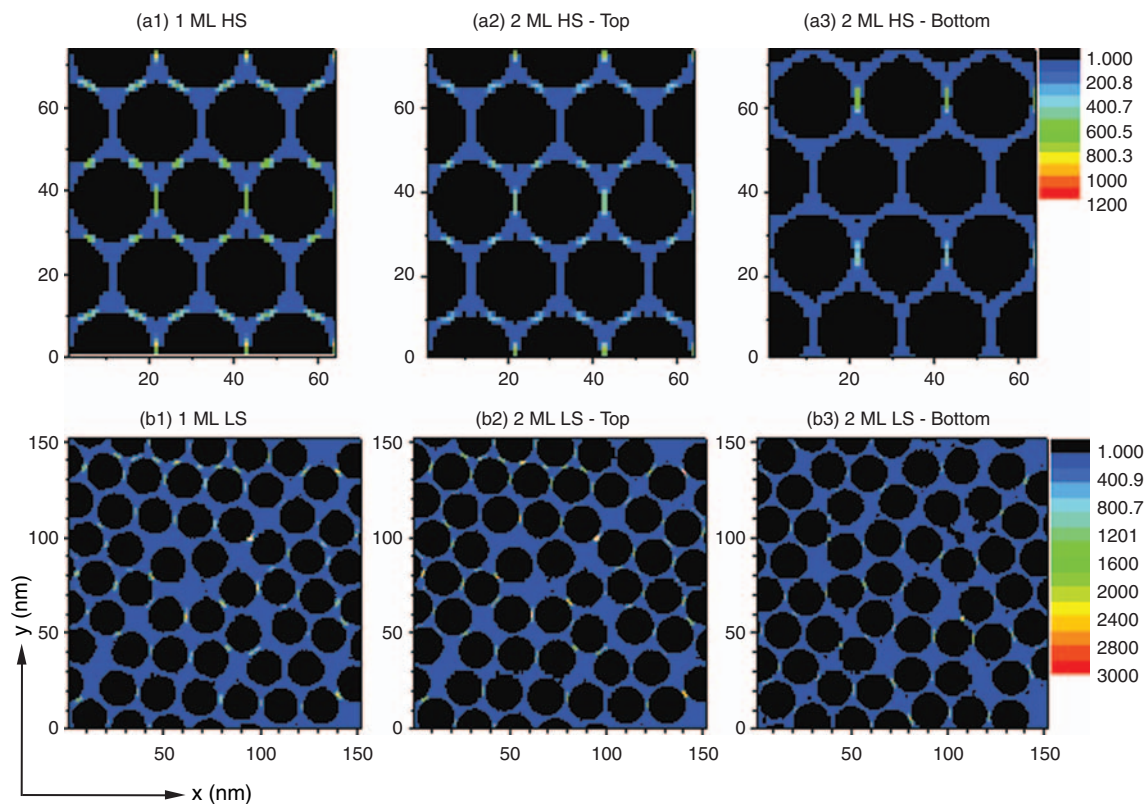
3.2. $\langle \mathbf{E}^2 \rangle$ Distribution

Figure 4 shows examples of the $\langle \mathbf{E}^2 \rangle$ distribution for the HS and LS assemblies. Only the 1 ML (Figs. 4(a1) and b1)) and the 2 ML (Figs. 4(a2, a3, b2, and b3)) assemblies are shown for the *x*-polarized incident light. For the 1 ML HS assembly, the high local fields were apparent at contact space cells between two spheres. For the 2 ML HS case, the local fields at the contact space cells in the top layer were also substantial, although they were reduced from that of the 1 ML case. The local fields were largely reduced at the bottom layer probably because only about 8% of the incident light penetrated through the top layer.

For the 1 ML LS assembly, the high local fields were apparent at some contact space cells between two spheres. While the contact space cells in the LS assemblies had a density lower than those in the HS assemblies, the local field intensities were higher. For the 2 ML LS assembly, the local fields at the contact space cells at the top layer were slightly reduced from those of the 1 ML assembly. The local fields at the bottom layer were as high as those at

the top layer, even though most of the incident light must have been extinguished after the top layer. In Figure 4, the $\langle \mathbf{E}^2 \rangle$ distributions between the two layers in the 2 ML assemblies were not presented since the local field intensities were negligible.

Figure 5 shows examples of the $\langle \mathbf{E}^2 \rangle$ distribution for the LR assemblies. The 2 ML assembly for the *x*-polarized light is shown. In the top layer (Fig. 5(a)), the high local fields were apparent at some contact space cells between two rods. Because of many side-by-side arrangements, the interparticle contact area of the LR assemblies was much larger than that of the HS or LS assemblies, generating higher local fields. The local fields were somewhat reduced at the bottom layer (Fig. 5(b)). However, the local field reduction at the bottom layer was not as much as the light extinction estimated from the transmission spectra of Figure 3, which may imply that interlayer coupling was in effect.

In Figure 5(c), the $\langle \mathbf{E}^2 \rangle$ distribution at the interlayer is shown. Unlike the cases of the HS and the LS assemblies, rather high local fields were apparent at some free interlayer spaces. The high local field spots at the interlayer were somewhat broadly shaped, while the interlayer contact must be line-shaped. Figure 5(d) shows the distribution of the *z*-component of the $\langle \mathbf{E}^2 \rangle$ at the interlayer. Figure 5(d)

Fig. 4. Maps of $\langle \mathbf{E}^2 \rangle$ distribution for the hexagonal close (HS) packed and random loose (LS) packed assemblies of 20 nm spheres: (a1) and (b1) *xy* cross-section ($z = 0$) in the 1 ML film; (a2) and (b2) *xy* cross-section of the top layer in 2 ML film; (a3) and (b3) *xy* cross-section of the bottom layer in the 2 ML film. Only the cases of *x*-polarized incident light are shown. Note that the color scale bars and the *xy* dimensions for the HS and the LS are not same.

RESEARCH ARTICLE
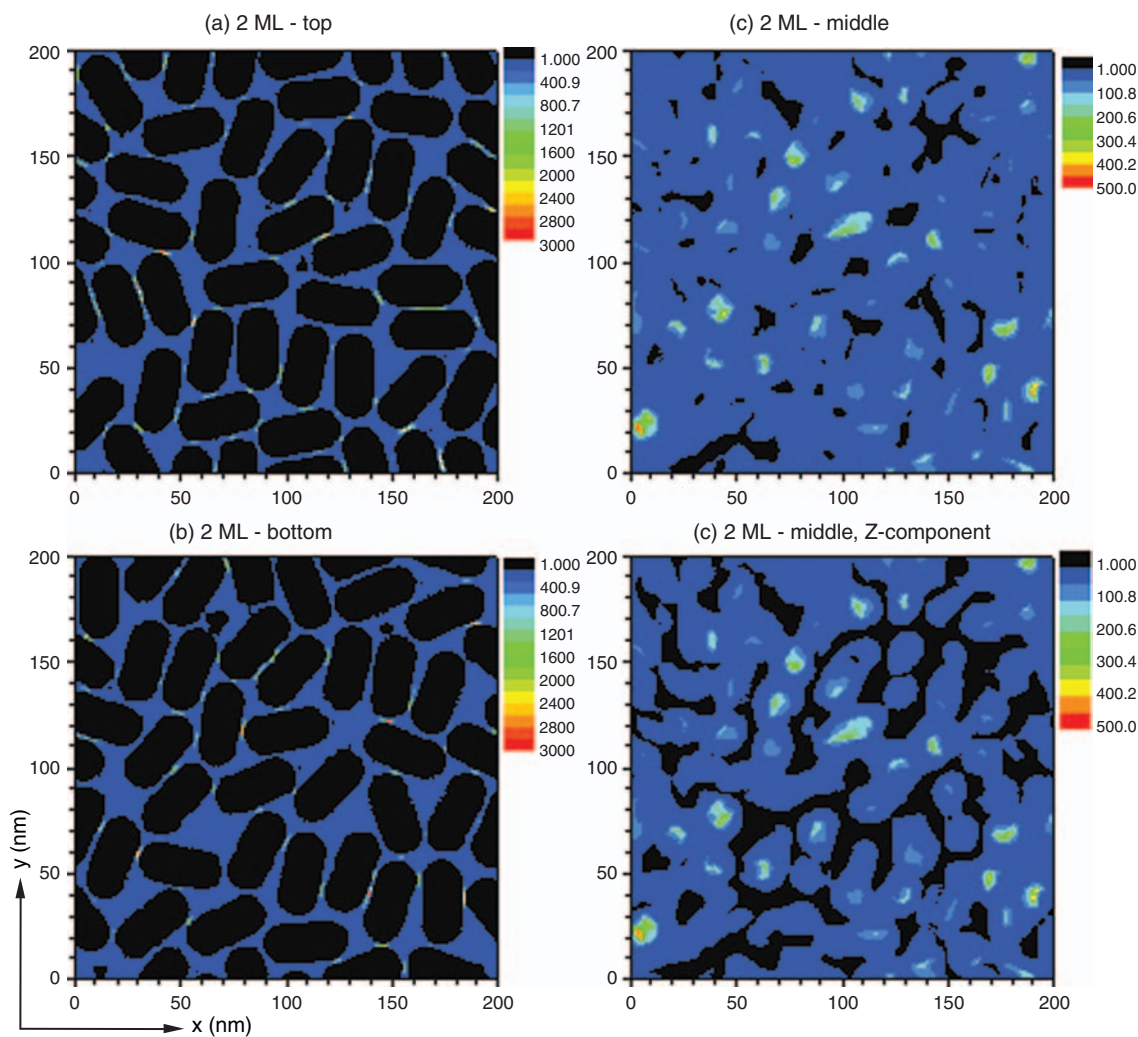
Fig. 5. Maps of $\langle \mathbf{E}^2 \rangle$ distribution for the random loose (LR) packed assemblies of 20 nm diameter, 41 nm length rods. The cases of the 2 ML film for *x*-polarized light are shown. (a) *xy* cross-section of the top layer; (b) *xy* cross-section ($z = 0$) of the interlayer, (c) *xy* cross-section of the bottom layer, (d) the map of $\sum \langle \mathbf{E}_z^2 \rangle$. Note that the color scale bars of plots (c) and (d) are different from (a) and (b).

is almost same as Figure 5(c), implying that the interlayer local fields were mostly *z*-polarized.

The $\langle \mathbf{E}^2 \rangle$ distribution of each target was then averaged in the *xy* cross-sectional plane. The average along the light propagation direction is shown in Figure 6. In Figure 6, the cases for the HS, LS and LR assemblies are shown in (a1–a4), (b1–b4), and (c1–c4), respectively. In each of the 1 ML cases (Figs. 6(a1, b1, c1)), there was a broad peak centered at $z = 0$, where the intralayer contacts between two spheres or two rods were made. In each of the 2 ML cases (Figs. 6(a2, b2, c2)), there were two such broad peaks. The peak at the positive *z* was for the top layer and the peak at the negative *z* for the bottom layer. Intensities of the bottom layer peaks are in general lower than those of the top layer peaks.

In each of the 2 ML cases, there was a sharp peak at $z = 0$, corresponding to the local fields produced at the interlayer contact. This peak is sharp and large in the

LR assemblies, but is relatively small in the HS and LS assemblies. The interlayer peaks of the 3 ML and 4 ML cases showed the same trend, reflecting the measure of interlayer contact in each target structure.

In each of the 3 ML (Figs. 6(a3, b3, c3)) and 4 ML (Figs. 6(a4, b4, c4)) cases, there were as many broad peaks as there were apparent layers. The intensities of these broad peaks decreased as the layer went to the bottom, since the incident light did not reach the bottom layers. The interlayer local fields for the LR assemblies were reduced accordingly.

The experimental extinction spectra of Figures 1(c and d) show Beer-Lambert type behavior; the optical density increased linearly with film thickness, implying that the light intensity distribution along the light propagation direction followed an exponential decay pattern. The penetration depths of the experimental films at 632.8 nm are estimated to be 1.03 ML for the NS films and 1.35 ML
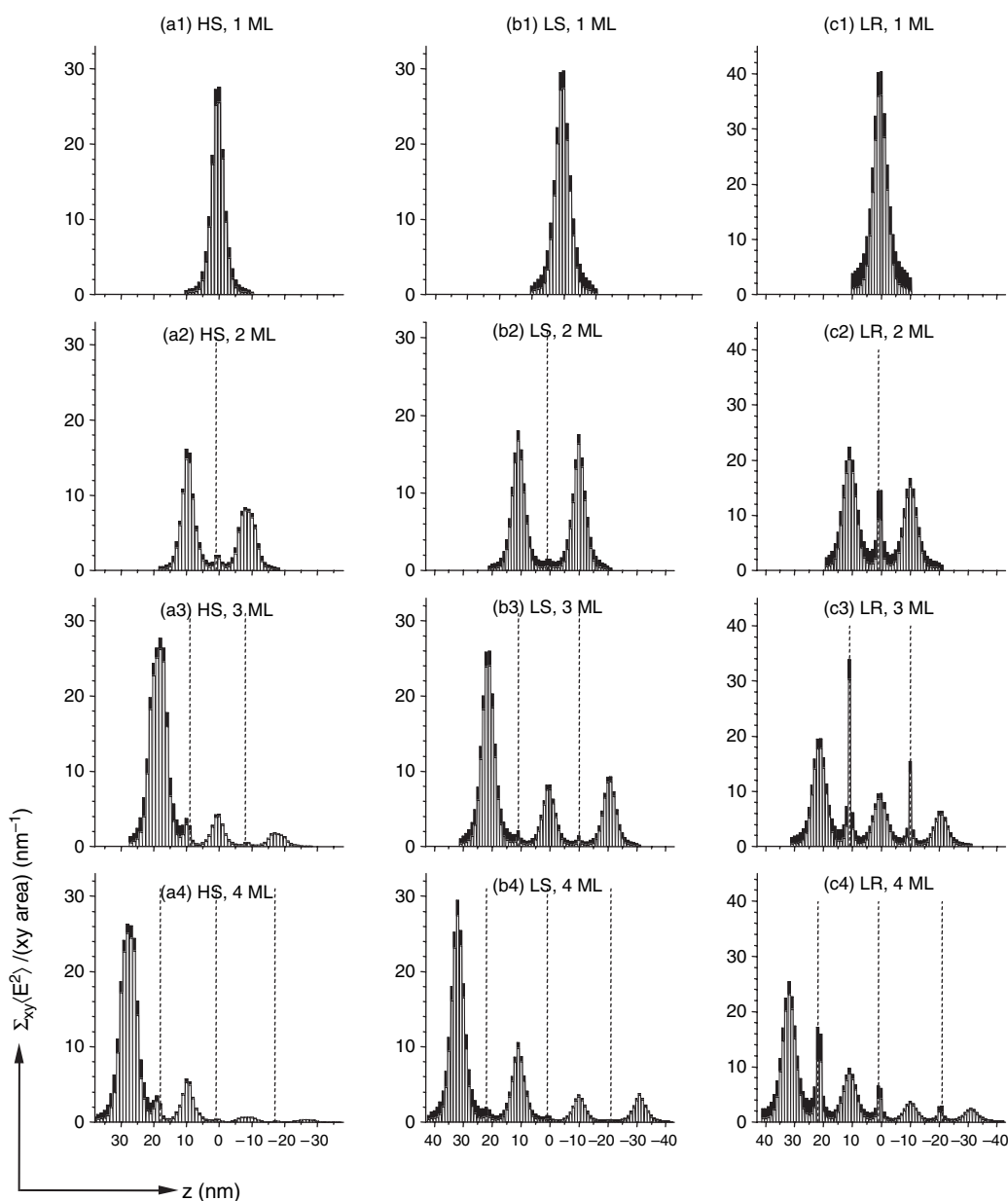
Fig. 6. Cross-sectional average of $\langle \mathbf{E}^2 \rangle$ along the *z*-axis:. (a1)–(a4) for the hexagonal closest packing of spheres; (b1)–(b4) for the random loose packing of spheres; (c1)–(c4) for the random loose packing of rods. In each bar graph, the white area is the contribution of the interface cells and the black area the contribution of other free cells around gold. Interlayers are marked with the dotted lines.

for the NR films. The simulated transmission spectra of Figure 3 showed slight deviations from Beer-Lambert type behavior. The sharp features in the Plasmon bands, especially for the 3 ML and 4 ML assemblies of the spheres, are partially responsible for the deviation. Because of higher optical densities in the simulated spectra than those in the experimental spectra, the penetration depths were estimated 30–50% shorter than the values in the experimental films. This estimation suggests that the cross-sectional local field distribution in 3 ML or 4 ML cases of Figure 6 reflects mostly the incident light intensity distribution along the light propagation direction. In contrast, in the 2 ML cases,

the local field distribution in the bottom layer is more close to that of the top layer than the estimated light field distribution indicates.

When the cross-sectional average of $\langle \mathbf{E}^2 \rangle$ is totaled over the *z* direction, the sum of average local field for the LR assemblies is larger than that for the LS or HS assemblies, which is consistent with the trend in the SERS experiments. The sum of the average local field in each target structure increases slightly as the number of layers increases. However, the increase is not as large as the SERS data. In the SERS experiments, the scattered radiation was collected into an upward direction so that

RESEARCH ARTICLE

the scattered radiation from the lower layers would have greatly reduced chance to escape the high optical density film. Considering this effect in evaluating Figure 6, only the top few layers would have contributed to the SERS signal.

3.3. Limitations of the FDTD-MEEP Calculation

There were several limitations in applying the FDTD-MEEP calculation to the presented system. For example, a field blow-out problem occurred on occasion. This is considered a computational artifact caused by combinations of the periodic boundary conditions and the imperfect PML. This problem was more severe as the volume or density of the target space increased or the wave propagation time lengthened. To avoid this, the distance from the light source to the target space had to be increased to 1.0 μm. Because of the dimension of the light propagating distance, the xy dimension and the spatial resolution had to be limited to compromise the memory size of the employed computer system.

Accordingly, the packing structures of spheres or rods in the presented calculations had limitations as they were to satisfy the periodic boundary conditions in the limited xy dimension. As a result, the surface density of spheres or rods in the LS or LR assemblies was lower than that of the corresponding experimental film. This would have caused a blue shift in the LSPR wavelengths in the simulated transmission spectra and decreased the local fields induced by interparticle Plasmon couplings. Additionally, layer-by-layer assembly had a limitation. In the experiments, spheres or rods of an upper layer would have preferred to sit at interstitial sites of the lower layer. However, this condition was not achieved in the computations for the LS or LR assemblies. As the result, the calculated interlayer coupling was insufficient to explain the trend of the SERS variation with the number of layers. The size of the contact spacing (1 nm) was the minimum cell size of this calculation and may be still larger than the closest interparticle gaps in the experimental films. This could be critical since the intensity of the local electric field increases dramatically as the interparticle distance is reduced.[4, 30]

Another limitation of the calculations herein is that the direction of the incident light did not fully satisfy the optical arrangement of the SERS setup. In the Raman spectrometer employed, the excitation laser was focused with a $50\times$ microscope objective lens with a numerical aperture of 0.75. The laser was incident with conically distributed angles as wide as 49°, while the calculation was made only for the normal incident. The Raman scattering was collected with the same objective lens as the incident excitation. The effects of this optical arrangement are discussed in the following section.

3.4. Interlayer Coupling

Figure 1(e) suggests that each layer in a multilayer film contributed almost equally to the SERS signal when the number of layers was less than a saturation layer. When the optical density is as high as the experimental films presented, such SERS behavior could be explained by a very efficient interlayer coupling.

The interparticle coupling is strong when the polarization direction of the light is parallel to the interparticle axis, and weak by an order of magnitude when it is perpendicular.[30, 31] Therefore, under the conditions of the calculations presented, the interlayer coupling induced directly by the incident light must be weak. In contrast, high local fields were calculated at the interlayers in the LR assemblies. The calculated interlayer local field was z-polarized as shown in Figure 5(d).

In Figure 7, the contributions of x-, y-, and z-components of electric fields in Figure 6(c2) are plotted. While the intralayer local fields were polarized transversely (x- or y-polarized), the interlayer local fields shown at $z = 0$ were longitudinally polarized (z-polarized). This implies that the intralayer local fields were generated by radiation-induced Plasmon coupling while the interlayer local fields by different coupling mechanism, most likely an electron-induced coupling. In the electron-induced coupling mechanism, an electron oscillation in one layer induces an oscillation of image charges in its neighboring layer. As the two oscillations are synchronized and out-of-phase, oscillating dipoles polarized along the interlayer direction are generated.

There are several SERS experiments[32, 33] and theoretical works[34–36] that are related to the interlayer coupling. In most of those works, a noble metal particle sitting on a flat noble metal film was the object of study, where the interlayer coupling is induced between localized surface Plasmon and delocalized surface Plasmon. The interlayer
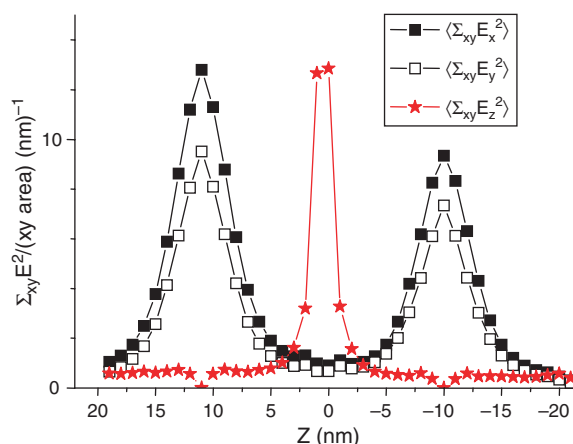
Fig. 7. Contributions of x-, y-, z-components in the cross-sectional average of $\langle \mathbf{E}^2 \rangle$ in the 2 ML LR assembly: -■-(black), x-component; -□-(black), y-component; -★-(red), z-component. The incident light was x-polarized.

coupling presented herein is similar to those works in that it is electron-induced via image charges but is a little different in that the interlayer coupling of this work is between quasi-localized surface Plasmons. In other words, the intralayer local fields are induced radiatively between localized surface Plasmons and are formed as hot spots at interparticle contacts as shown in Figures 4, 5(a, b), while the electron-induced interlayer local fields are rather spread as shown in Figures 5(c and d).

We suppose that the local fields in the lower layers can be amplified by an action of electron-induced image charges over the layers in a cascade way. If this process occurs effectively, the electron oscillations in the lower layers may follow those in the top layer. Then, the overall local field would be approximately equal to the contribution of the top layer multiplied by the number of layers. This hypothesis can explain the observations of the SERS variation with the number of layers.[7, 10, 11]

On the contrary, the local field distributions in Figure 6 do not support the above hypothesis. However, the electron-induced coupling may be spread over the layers in much slow time scale. We tested this possibility by packing spheres and rods in a two-dimensional *xz* space, and monitored the local field distributions similar to Figure 6 for a very long time. No appreciable changes in the local field distributions are found up to 6000 TU (=20 ps). If the spread of the electron-induced coupling over the layers is truly working, it must occur in much slower time scale than the computation of this work can access.

Finally, the effects of the optical arrangement of the Raman spectrometer are considered. The focusing lens of the employed Raman spectrometer provided a wide distribution of incident angles, which would have increased the *z*-polarized interlayer local field via radiation-induced coupling mechanism. The *z*-polarized Raman scattering would have not been detected if the detection had been made normal to the target surface. However, the latter effect must have been relaxed since the collection angle of our Raman spectrometer was as wide as 49°. The two effects, caused by the angles of the incidence and collection in the Raman spectrometer, work in opposition with regards to the relative contributions of polarization states of the scattered light.

4. CONCLUSIONS

The results of the FDTD calculations have shown that both intralayer and interlayer couplings are greater in the NR assemblies than the NS assemblies, in accord with the SERS experiments. This phenomenon is explained mainly by a larger interparticle contact area in the NR assemblies. However, because of computational limitations in establishing the target space, the local field distribution over the layers and the strength of the interlayer coupling was not sufficient to explain the variations in SERS intensity

with the number of layers. Nevertheless, high local fields were found at the interlayers in the NR assemblies. The interlayer local field was polarized differently from the intralayer local field and is thought to be induced not by direct interaction with the light field, but by secondary coupling between conduction electrons in two layers. The interlayer coupling is thought to work as a channel for local field spread over the layers, although this was not verified. It is likely that, if the interlayer contact is made more closely in computation, the interlayer local field is increased and more contribution to the SERS signal from the lower layers can be expected.

References

1. N. Liver, A. Nitzan, and J. I. Gersten, *Chem. Phys. Lett.* 111, 449 (**1984**).
2. J. K. Bosnick, M. Maillard, and L. Brus, *J. Phys. Chem. B* 107, 9946 (**2003**).
3. D. P. Tsai, J. Kovacs, Z. Wang, M. Moscovits, V. M. Shalaev, J. S. Suh, and R. Botet, *Phys. Rev. Lett.* 72, 4149 (**1994**).
4. H. J. Garcia-Vidal and J. B. Pendry, *Phys. Rev. Lett.* 77, 1163 (**1996**).
5. E. C. Le Ru, P. G. Etchegoin, and M. Meyer, *J. Chem. Phys.* 125, 204701 (**2006**).
6. H. Y. Jung, Y.-K. Park, S. Park, and S. K. Kim, *Anal. Chim. Act.* 602, 236 (**2007**).
7. S. Yun, Y.-K. Park, S. Park, and S. K. Kim, *Anal. Chem.* 79, 8584 (**2007**).
8. Y.-K. Park, S.-H. Yoo, and S. Park, *Langmuir* 23, 10505 (**2007**).
9. Y.-K. Park and S. Park, *Chem. Mater.* 20, 2388 (**2008**).
10. M. Oh, S. Yun, S. K. Kim, and S. Park, *Anal. Chim. Act.* 649, 111 (**2009**).
11. S. Yun, M. Oh, S. K. Kim, and S. Park, *J. Phys. Chem. C* 113, 13551 (**2009**).
12. A. Taflove and S. C. Hagness, Computational Electrodynamics: The Finite-Difference Time-Domain Method, 3rd edn., Artech House Publishers (**2005**).
13. K. S. Kunz and R. J. Luebbers, The Finite Difference Time Domain Method for Electromagnetics, CRC Press (**1993**).
14. K. S. Yee, *IEEE Trans. Antennas Propag.* AP-14, 302 (**1966**).
15. M. Futamata, Y. Maruyama, and M. Ishikawa, *J. Phys. Chem. B* 107, 7607 (**2003**).
16. T. Laroche and C. Girard, *Appl. Phys. Lett.* 89, 23319 (**2006**).
17. C. Charnay, A. Lee, S.-Q. Man, C. E. Moran, C. Radloff, R. K. Bradely, and N. J. Halas, *J. Phys. Chem. B* 107, 7327 (**2003**).
18. H. Tamaru, H. Kuwata, H. T. Miyazaki, and K. Miyano, *Appl. Phys. Lett.* 80, 1826 (**2002**).
19. P. Behere, S. K. S. M. Ajay Ram, V. S. Muthukumar, and K. Venkataramaniah, *Int. J. Phys. Sci.* 4, 250 (**2009**).

RESEARCH ARTICLE

20. S. A. Maier, P. G. Kik, and H. A. Atwater, *Phys. Rev. B* 67, 205402 (**2003**).
21. C.-L. Zhan, X.-F. Ren, Y.-F. Huang, K.-M. Duan, and G.-C. Guo, *Chin. Phys. Lett.* 25, 559 (**2008**).
22. Y. Chu, E. Schonbrun, T. Yang, and K. B. Crozier, *Appl. Phys. Lett.* 93, 181108 (**2008**).
23. C. Oubre and P. Nordlander, *J. Phys. Chem. B* 108, 17740 (**2004**).
24. F. Hao and P. Nordlander, *Chem. Phys. Lett.* 446, 115 (**2007**).
25. S. C. Johnson, MIT electromagnetic equation propagation, available from http://ab-initio.mit.edu/wiki/index.php/Meep.
26. J.-P. Berenger, *J. Compt. Phys.* 114, 185 (**1994**).
27. P. B. Johnson and R. W. Christy, *Phys. Rev. B* 6, 6 (**1972**).
28. A. Vial, A.-S. Grimaut, D. Macías, D. Barchiesi, and M. L. de la Chapelle, *Phys. Rev. B* 71, 085416 (**2005**).
29. A. Farjadpour, D. Roundy, A. Rodriguez, M. Ibanescu, P. Bermel, J. D. Joannopoulos, and S. G. Johnson, *Opt. Lett.* 31, 2972 (**2006**).
30. E. Hao and G. C. Schatz, *J. Chem. Phys.* 120, 357 (**2004**).
31. H. Xu and M. Käll, *ChemPhysChem.* 4, 1001 (**2003**).
32. J. K. Yoon, K. Kim, and K. S. Shin, *J. Phys. Chem. C* 113, 1769 (**2009**).
33. W.-H. Park, S.-H. Ahn, and Z. H. Kim, *ChemPhysChem.* 9, 2491 (**2008**).
34. F. Le, N. Z. Lwin, J. M. Steele, M. Käll, N. J. Hallas, and P. Nordlander, *Nano Lett.* 5, 2009 (**2005**).
35. P. Nordlander and F. Le, *Appl. Phys. B* 84, 35 (**2006**).
36. A. Christ, T. Zentgraf, S. G. Tikhodeev, N. A. Gippius, O. J. F. Martin, J. Kuhl, and H. Giessen, *Phys. Stat. Sol. B* 243, 2344 (**2006**).

RESEARCH ARTICLE

10

J. Comput. Theor. Nanosci. 7, 1–10, **2010**